Roughening Dynamics of Interfaces in the Two-Dimensional Quantum Ising Model

Wladislaw Krinitsin,[1,2,*,†] Niklas Tausendpfund,[1,3,*] Matteo Rizzi,[1,3] Markus Heyl,[4,5] and Markus Schmitt[1,2]

[1]Institute of Quantum Control (PGI-8), Forschungszentrum Jülich, D-52425 Jülich, Germany
[2]Faculty of Informatics and Data Science, University of Regensburg, D-93040 Regensburg, Germany
[3]Institute for Theoretical Physics, University of Cologne, D-50937 Köln, Germany
[4]Theoretical Physics III, Center for Electronic Correlations and Magnetism, Institute of Physics, University of Augsburg, D-86135 Augsburg, Germany
[5]Centre for Advanced Analytics and Predictive Sciences (CAAPS), University of Augsburg, Universitätsstraße 12a, 86159 Augsburg, Germany

(Received 8 January 2025; accepted 21 May 2025; published 20 June 2025)

The properties of interfaces are key to understanding the physics of matter. However, the study of quantum interface dynamics has remained an outstanding challenge. Here, we use large-scale tree tensor network simulations to identify the dynamical signature of an interface roughening transition within the ferromagnetic phase of the 2D quantum Ising model. For initial domain wall profiles we find extended prethermal plateaus for smooth interfaces, whereas above the roughening transition the domain wall decays quickly. Our results can be readily explored experimentally in Rydberg atomic systems.

DOI: 10.1103/9bsk-x9rw

Introduction—The static and dynamical properties of interfaces are fundamental to understanding the physics and to engineer the functionality of materials. Interfaces can even undergo their own unique phase transitions independently of the bulk matter. At a roughening transition, first identified in models for surface growth and classical magnetism [1–3], the nature of interfaces changes qualitatively from being smooth to rough. Intuitively these different phases can be characterized by their interface fluctuations, with small bounded fluctuations in the smooth phase and large unbound ones in the rough phase. The theoretical analysis of effective solid-on-solid (SOS) models revealed the Berezinskii-Kosterlitz-Thouless (BKT) nature of the transition [4,5], which was confirmed in numerical simulations [6]. For experimental studies, the interface between liquid and crystallized Helium-4 is a particularly suited model system [7]. At the involved low temperatures, however, quantum effects enter. It was found that quantum fluctuations can cause a roughening transition at vanishing temperature $T = 0$ in two-dimensional systems, but not in three dimensions [8,9]. Interface properties are relevant also in a broader scientific context beyond condensed matter. For instance, in high-energy physics, the flux tube connecting quarks realizes an interface that can undergo roughening [10]. Signatures of which were recently observed via digital quantum simulation of a lattice gauge theory [11]. The exploration of such interface roughening in quantum matter *away from equilibrium* has, however, remained an outstanding challenge to date.

In this Letter, we study the nonequilibrium signatures of the roughening transition in the quantum Ising model. Based on large-scale Tree Tensor Network (TTN) simulations for real-time evolution [12–14], we find that the underlying quantum roughening transition is reflected in a qualitative change of dynamical behavior of domain wall initial conditions upon tuning the transverse field strength. In particular, we identify the independent equilibration of the interface in the smooth interface regime as an alternative cause of prethermal plateaus, which is distinct from the known mechanisms relying on approximate conservation laws or Hilbert space fragmentation [15,16]. The phenomenology can be readily explored in experiments with Rydberg atomic systems [17–31].

Model—For the central objective to study the dynamics of interfaces we consider the paradigmatic transverse-field Ising model (TFIM) on a square lattice, given by

$$\mathrm{H} = -J\sum_{\langle i,j\rangle}\sigma_i^x\sigma_j^x - g\sum_i \sigma_i^z, \tag{1}$$

where the first sum runs over all neighboring spin pairs. The TFIM exhibits a ferromagnetic phase, which extends to nonzero temperatures, with a quantum phase transition at $g_c/J \approx 3.04$ and a thermal transition temperature of $T_c/J \approx 2.27$ at $g = 0$ [32]. Importantly, the 2D quantum Ising model inherits a second quantum phase transition

*These authors contributed equally to this work.
†Contact author: w.krinitsin@fz-juelich.de

point of BKT type within the ferromagnetic phase, which is associated with a transition from smooth to rough interfaces [9]. A suited order parameter will be defined at a later point of this Letter, providing a quantitative description of the transition. In the quantum domain, when considering the limit $J \gg g$, the TFIM can be perturbatively linked to the PXP model, which shows strong dynamical constrains and Hilbert space fragmentation, leading to a slow relaxation of various domain wall initial conditions [13,14,33,34].

For the purpose of studying the dynamics of quantum interfaces, we will initialize the system with two oppositely polarized magnetic domains, separated by a straight domain wall; see Fig. 1(a). This is a natural choice for experimental platforms, while not introducing any additional effects stemming from, e.g., interface curvature. For weak enough transverse fields, i.e., within the PXP approximation, these states remain stable due to sectors of different interface lengths being dynamically disconnected from each other, preventing thermalization up to timescales that scale exponentially with J/g. (Eventual thermalization is expected to happen for transverse fields $g/J \geq 0.2$ as is revealed by an analysis of the level-spacing statistics of a 4×5 system; see SM for more details [35], which includes Refs. [36,37].)

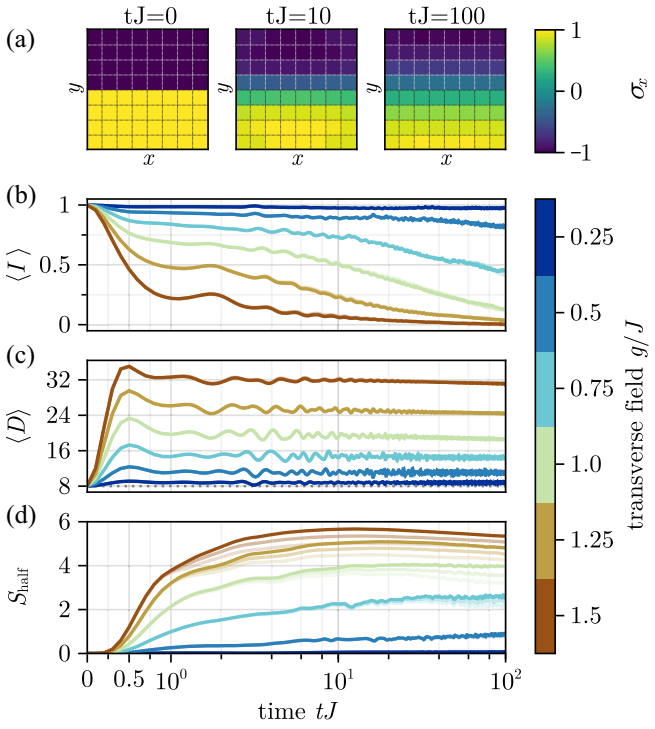

FIG. 1. Time evolution of a flat interface on an 8×8 lattice with open boundary conditions. (a) Spatially resolved magnetizations at times $tJ = 0$, 10, and 100 for a transverse field of $g/J = 0.75$. The bottom three plots show (b) the imbalance, (c) the domain wall length, and (d) the entropy of entanglement across the initial interface for several transverse fields: the color coding is indicated in the color bar to the right. The imbalance shows the existence of long-lived plateaus, even at transverse fields $g \approx J$. All the results are shown for three different bond dimensions $\chi = 181$, 256, 362, where the opacity increases with the bond dimension. For panels (a) and (b), almost all of the data points lie on top of each other.

In the following we depart from any such perturbative limit and target the dynamics in strongly correlated regimes $g/J \sim 1$. As will be shown later, we observe prethermal plateaus that cannot be explained by Hilbert space fragmentation. Instead, this nonperturbative effect is related to the thermalization of the interface below a roughening temperature.

Numerical methods—In order to comprehensively explore the quantum roughening dynamics, we employ a variety of complementary tensor network techniques. The simulations of the full dynamics on the 2D lattice were performed using TTNs and the time-dependent variational principle [12–14]. Being loop-free, TTNs are efficiently contractible and their hierarchical structure allows for a more natural covering of the 2D lattice than the widely used matrix product states (MPSs) [38]. MPSs will be used later in the text in order to solve time evolution of an effective 1D model. Furthermore, we utilize the variational uniform matrix product state (VUMPS) algorithm [39–41] to study the ground state properties of the effective model in the thermodynamic limit. Quantum Monte Carlo (QMC) simulations [42–44] are employed to estimate effective temperatures corresponding to the domain wall initial conditions. More details on the aforementioned methods are given in Supplemental Material (SM) [35].

Interface dynamics—A first indication for the slow thermalization dynamics is provided by the time evolution of the magnetization imbalance,

$$I = M_T - M_B, \tag{2}$$

with $M_{T/B} = (1/N) \sum_{i \in T/B} \sigma_i^x$ and T/B indicating the top and bottom halves of the system [see Fig. 1(a)]. The imbalance is maximal in the initial state $\langle I(t=0) \rangle = 1$ and it has to vanish in a thermal state. Figure 1(b) shows $\langle I(t) \rangle$ for a range of transverse fields; the spatially resolved magnetization $\langle \sigma_i^x(t) \rangle$ at three time points is included exemplarily in Fig. 1(a). For the largest transverse fields we expect a rapid thermalization, which is reflected by the observed rapid drop in the imbalance on a timescale of $tJ \approx 1$. The subsequent slow decay of the remaining imbalance is attributed to the diffusive approach to a finally homogeneous energy density. The smallest field values conversely show extremely long-lived nonthermal states due to the aforementioned emergent constraints [33,34]. Noticeably, however, prethermal plateaus seem to dominate the dynamics even up to intermediate values of the transverse fields of up to $g/J \approx 1$ and timescales of $Jt \approx 10$.

The fact that the domain wall length operator $D = \frac{1}{2} \sum_{\langle i,j \rangle} (1 - \sigma_i^x \sigma_j^x)$ shown in Fig. 1(c) strongly departs from its initial value highlights, that the existence of

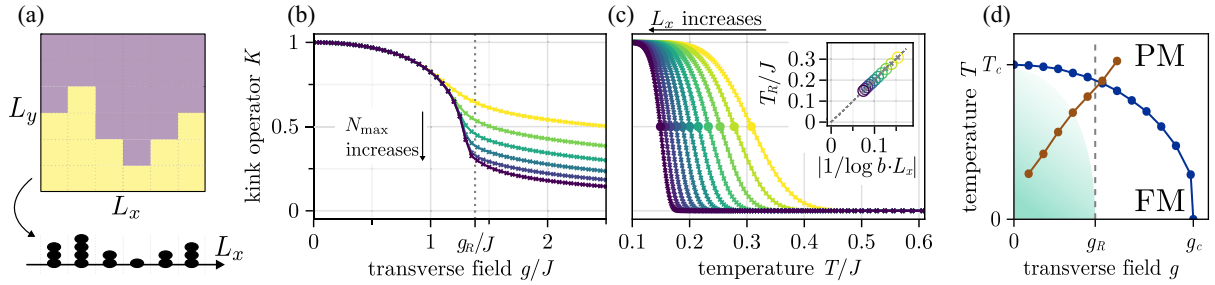

FIG. 2. (a) Mapping from a domain wall state in the full two-dimensional model to an effective one-dimensional bosonic state. (b) Expectation value of the kink operator, evaluated on the ground state of the effective model as a function of the transverse field. Different maximal occupation numbers $4 \leq N_{\max} \leq 14$ in steps of two are shown; as $N_{\max}$ increases, the kink operator starts exhibiting a jump at $g_R/J \approx 1.38$ corresponding to the roughening transition; see also SM [35]. (c) Expectation value of the kink operator, evaluated on the thermal state of the effective model in the classical limit ($g = 0$) as a function of temperature. We consider chain lengths $L_x \in [500, 512 \times 10^3]$, with exponentially increasing steps. The inset shows that the crossover temperature T_R, defined by $\langle K(T_R/J)\rangle = 0.5$, vanishes in the thermodynamic limit as the inverse logarithm of the system size, confirming the analytical prediction (5) that is indicated by the dashed gray line. The constant b in the x axis label is given by $b = 2(1 - \cos 1)/\log 2$. Data points in (b) and (c) are represented by crosses, with a linear interpolation between them. (d) Phase diagram of the 2D TFIM. The blue line represents the critical line separating the ferro- from the paramagnetic phase, the red line denotes the effective temperature of the initial state based on its energy, obtained from QMC simulations; see SM [35]. Our results point toward the existence of a roughening transition at a value of $g_R/J \approx 1.38 < g_c/J$. The green shaded region shows the extended smooth interface regime present in finite systems.

prethermal plateaus at intermediate transverse fields cannot be captured within the usual framework of Hilbert space fragmentation governed by restricted domain wall lengths. We will instead demonstrate in the following that an effective description can be formulated in terms of a single-domain-wall approximation.

Figure 1 includes a convergence check of the numerical results with different bond dimensions up to $\chi = 362$. While late times and stronger transverse fields become challenging, the prominent prethermal plateaus are well within the regime of certain convergence. Most sensitive to varying bond dimension is the half-system entanglement entropy [Fig. 1(d)], when splitting the system into two equal partitions along the initial interface, which shows that the moderate amounts of entanglement generated up to the lifetime of the plateaus are well captured.

Effective model—In order to explain the observed nonperturbative prethermal effects, we formulate an effective, one-dimensional model that corresponds to the projection of Eq. (1) onto the subspace of domain wall states with exactly one horizontal interface segment per column (see SM for a more detailed derivation [35]),

$$\mathrm{H}_{\mathrm{eff}} = 2J \cdot \sum_i |N_i - N_{i+1}| - g \cdot \sum_i \left(E_i + E_i^\dagger\right). \quad (3)$$

Here, we introduced height operators N_i measuring the perpendicular displacement of the domain wall; see Fig. 2(a). The raising (lowering) operators $E_i^\dagger (E_i)$ are the projection of the σ_i^z, which in the manifold of single horizontal domain walls can only flip spins next to the domain wall. The raising and lowering operators obey the commutation relations $[E_i, N_j] = E_i \delta_{i,j}$ similar to the standard definition used in quantum rotor models [45]. Hence, the phase operator φ defined through $E_j = \exp(i\varphi_j)$ is canonically conjugate to the height operator and the N_i can alternatively be viewed as bosonic occupation number operators. It is important to note that the model is not based on some low-order Schrieffer-Wolff transformation, but instead captures the relevant fluctuations of the initial domain wall.

The effective model (3) is also closely related to SOS-like models [4,5], in which roughening appears as a BKT transition [46]. The critical point of $\mathrm{H}_{\mathrm{eff}}$ has been argued to be upperbounded by the critical point of the quantum rotor model [47–49]. This is noticeably below the symmetry-breaking phase transition of the full TFIM.

Roughening is indicated by the kink operator

$$K_\alpha(l) = \cos[\alpha(N_1 - N_l)], \quad (4)$$

which probes the fluctuations of the interface in the direction perpendicular to its initial orientation. It is a suited order parameter because a value of $\langle K_\alpha(l)\rangle = 1$ corresponds to a flat (smooth) interface, while a value of $\langle K_\alpha(l)\rangle = 0$ corresponds to a highly fluctuating (rough) interface. A universal quantitative analysis would require taking the limits $\lim_{\alpha\to 0}\lim_{l\to\infty}\langle K_\alpha(l)\rangle$ for the angle α and distance l. In our numerical analysis of finite systems, we choose $l = L_x$ maximal and we find that $\alpha = 1$ is the minimal value, that sufficiently suppresses bulk contributions when considering the full TFIM; see SM [35] for more details. From now on we will drop the dependency on α and l, i.e., $K \equiv K_{\alpha=1}(l = L_x)$.

Figure 2(b) shows the ground state expectation value of the kink operator for varying g/J and different values of the occupation number truncation $N_{\max}$, obtained using the VUMPS algorithm. The drop of $\langle K\rangle$ with increasing g/J clearly indicates the transition from a smooth to a rough interface regime. This drop becomes sharper as $N_{\max}$ is increased, pointing toward the existence of a phase transition—a fit of the correlation length provides the critical value $g_R/J \approx 1.38$. Further analysis strengthens the hypothesis of a BKT transition in the SOS model; see End Matter and SM [35].

Next, we turn toward the question of whether its signatures survive even at nonzero temperatures T. Note that order at $T > 0$ would not violate the Mermin-Wagner theorem due to the infinite local Hilbert space dimension [50]. We consider the classical limit of the effective model, i.e., $g/J = 0$, and use a transfer matrix based method to calculate the expectation value of the kink operator in the thermal state; see End Matter and SM for more details [35]. The thermal expectation value of the kink operator shown in Fig. 2(c) exhibits an extended regime with a clear signature of smooth interfaces at low temperatures for system sizes up to $L_x = 5 \times 10^5$. However, the turning point shifts with increasing system size and its location behaves perturbatively as

$$T_R/J = 2\log\left(\frac{2[1-\cos(\alpha)]L_x}{\log(2)}\right)^{-1}. \tag{5}$$

See the inset of Fig. 2(c) as well as End Matter and SM [35], which includes Ref. [51]. Thus, in the thermodynamic limit $L_x \to \infty$, roughening occurs immediately for any $T > 0$. Nonetheless, clear signatures of a smooth interface regime at nonzero temperature survive up to very large system sizes due to the logarithmic dependence of T_R on L_x, which has especial relevance for current experimental realizations in quantum simulators.

Figure 2(d) shows a sketch of the inferred phase diagram in the full two-dimensional Ising model, summarizing all the previously discussed results: The ferromagnetic phase encompasses an extended smooth interface regime delimited by a roughening quantum phase transition (QPT) and a system-size dependent crossover at nonvanishing temperatures. We include the effective temperatures fixed by the domain wall initial condition for the range of considered transverse fields g/J, indicating that signatures of a smooth interface regime will vanish already at field strengths below the critical g_R. Concerning the nonequilibrium dynamics, this phase diagram suggests that the effective model can thermalize in the smooth domain wall regime, implying stability of domain walls for long times. We will show next that this prediction is even quantitatively accurate for the full dynamics of the two-dimensional TFIM.

Dynamical signature of roughening—The effective model covers the subspace of single domain wall states

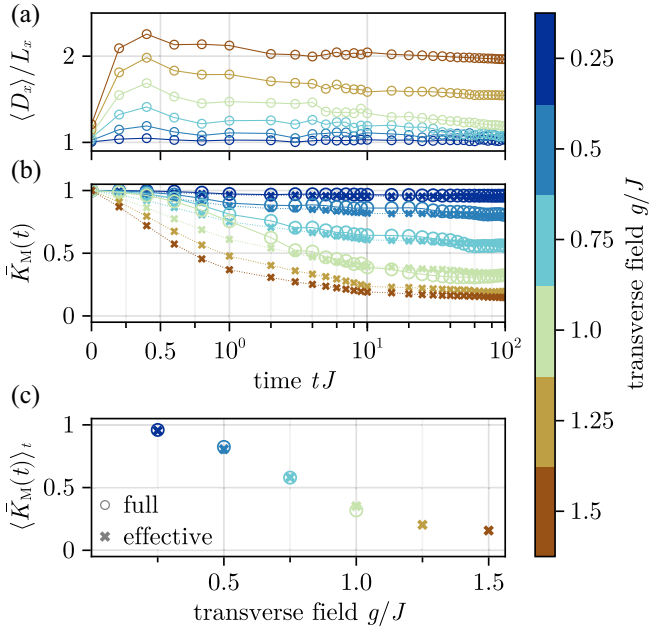

FIG. 3. (a) Time evolution of the horizontal contribution to the domain wall length divided by the horizontal lattice dimension. The plot shows that up until $g/J = 1$, each column has approximately one horizontal domain wall for the times considered, confirming the validity of the effective model (3) in that regime. (b) Comparison between the effective (dashed lines and crosses) and the full model (solid lines and circles) for the time evolution of the kink operator. In order to filter out the strong fluctuations of the data we show the running mean of the kink operator. For the full model, we calculate the modified kink operator $K_M = \langle K\rangle/\langle K_{\text{bulk}}\rangle$. We do not show data for transverse fields beyond $g/J = 1$, as bulk and interface contributions become increasingly difficult to disentangle. (c) Late-time averages of the kink operators shown in (b), taken over the interval $tJ \in [20, 100]$, as functions of the transverse field. The values agree well up to $g/J = 1$, once again confirming the quantitative predictive power of the effective model in that regime.

without bubbles or overhang. To check the validity of this description, we plot the time dependence of the horizontal domain wall length $D_x = 1/2\sum_{i,j}(\mathbb{1} - \sigma^x_{i,j}\sigma^x_{i,j+1})$ in Fig. 3(a). The small deviations of $\langle D_x\rangle/L_x$ from 1 for transverse fields up to $g/J \approx 1$ support the validity of the effective model in that regime.

We now turn to a direct comparison between the dynamics of the full and the effective model—the latter simulated using MPS. In the full 2D TFIM, the operator probing the vertical position of the domain wall at site i is given by $N_i = \sum_{j\perp i} j/2(\mathbb{1} - \sigma^x_{i,j}\sigma^x_{i,j+1})$ with the sum running over all lattice sites j perpendicular to the domain wall. For a meaningful comparison with the effective model, however, we need to account for bulk contributions such as single spin flips away from the domain wall. For that purpose, we define a modified kink operator $K_M = \langle K\rangle/\langle K_{\text{bulk}}\rangle$, where $\langle K_{\text{bulk}}\rangle$ is obtained by calculating the kink operator for a system where the interaction

along the initial domain wall is removed, i.e., only bulk effects contribute to the time evolution. Since the time-dependent expectation values obtained from the full and the effective models differ in their high frequency fluctuations, we will moreover consider their running time averages $\bar{K}(t) = (1/t)\int_0^t dt\langle K(t)\rangle$ instead for the direct quantitative comparison. See SM for more details [35].

The time evolution of the modified kink operator in comparison with the kink operator of the effective model is shown in Fig. 3(b). Data for the full model is restricted to transverse fields $g/J \leq 1$, since the separation of bulk from interface effects becomes infeasible for larger fields. We find very good quantitative agreement between these two models, meaning that the dynamics of interfaces in the TFIM can be understood in terms of the SOS model: for the considered intermediate values of the transverse field, the SOS model thermalizes within the smooth interface regime [cf. Fig. 2(d)] and the initially flat domain wall profile remains eternally stable. This stability of the domain wall manifests itself in the full TFIM in the form of prethermal plateaus with $\bar{K}_{\mathrm{M}}(t) > 0$. In contrast to the effective model, a subsequent decay of these prethermal states is to be expected in the full model, but these timescales seem out of reach for current numerical approaches. Figure 3(c) displays the late-time stationary values of the running, time-averaged kink operator by taking the mean over points lying in the interval $tJ \in [20, 100]$, which once more highlight the compelling quantitative agreement between the SOS model and the TFIM. Results obtained for a 16×16 lattice confirm said agreement for larger system sizes, without the need to suppress temporal fluctuations via taking the running mean; see SM [35] for more details. Finally, notice that the imbalance in Fig. 1(b) and the kink operator in Fig. 3(b) exhibit different lifetimes of the prethermal plateaus. This indicates that restoring the rotational symmetries requires longer times than the restoration of translational symmetry.

Discussion—Our analysis establishes a connection between the roughening transition and the relaxation dynamics of quantum interfaces in the 2D TFIM. The stability of domain walls in the smooth interface regime constitutes a new mechanism for prethermalization beyond known ones like proximity to an integrable point [15] or Hilbert space fragmentation and quantum scars [16], highlighting a qualitative change within the dynamical phase diagram of the TFIM in two dimensions.

The domain wall dynamics of the quantum Ising model can be probed experimentally in state of the art Rydberg atomic systems [31,52–54]. Domain wall initial conditions can be prepared via programmable locally controlled light shifts, and recent experiments demonstrate the feasibility of a transversely oriented magnetic field of the required intermediate magnitude [31,53]. Our formulation of the effective model remains unchanged for the typical antiferromagnetic interactions. Since the imbalance and the kink operator are immediately accessible through snapshot measurements, we expect that the described phenomenology is readily accessible in current Rydberg atom quantum simulators. An exciting prospect would be the possibility to probe longer timescales in this way.

Furthermore, it will be interesting to investigate other initial domain wall configurations in the light of roughening. Examples include the observed self-straightening dynamics of a initial zigzag configuration [31] and potential implications for false vacuum decay probed via bubble formation [55–58]. More generally, the impact of curvature on the phenomenology of the roughening dynamics remains to be explored in a future work. Another immediate question concerns the generalization to other symmetries, since the results presented here rely on a $\mathbb{Z}_2$ symmetry-broken phase.

The TTN simulations presented in this Letter were produced with TTN.jl [59], a software package we developed based on the ITensor library [60]. The MPS simulations were performed with the help of ITensor. The QMC simulations were produced with the help of the ALPS software package [61] and a rust library [44].

Acknowledgments—We acknowledge fruitful discussions with A. Segner, J.-D. Urbina, M. Steinhuber, L. Behringer, S. Tomsovic, T. Mendes-Santos, A. Gambassi, and U.-J. Wiese. M. S. and W. K. were supported through the Helmholtz Initiative and Networking Fund, Grant No. VH-NG-1711. We acknowledge support from the Deutsche Forschungsgemeinschaft (DFG) under Germany's Excellence Strategy-Cluster of Excellence Matter and Light for Quantum Computing (ML4Q) EXC 2004/1–390534769 (NT, MR and MS), under Grant No. 277101999—CRC network TR 183 (NT and MR), under Project No. 499180199—FOR 5522 (MH). M. H. has received funding from the European Research Council (ERC) under the European Union's Horizon 2020 research and innovation programme (Grant Agreement No. 853443). M. R. and N. T. acknowledge funding under Horizon Europe programme HORIZON-CL4-2022-QUANTUM-02-SGA via the Project No. 101113690 (PASQuanS2.1). The authors gratefully acknowledge the Gauss Centre for Supercomputing e.V. [62] for funding this project by providing computing time through the John von Neumann Institute for Computing (NIC) on the GCS Supercomputer JUWELS [63] at Jülich Supercomputing Centre (JSC) under grant NeTeNeSyQuMa. They also gratefully acknowledge computing time on the supercomputer JURECA [64] at Forschungszentrum Jülich under grants NeTeNeSyQuMa and pgi8.

Data availability—The data that support the findings of this article are openly available [65].

[1] W. K. Burton, N. Cabrera, and F. C. Frank, The growth of crystals and the equilibrium structure of their surfaces, Phil. Trans. R. Soc. A **243**, 299 (1951).

[2] R. L. Dobrushin, Gibbs state describing coexistence of phases for a three-dimensional Ising model, Theory Probab. Appl. **17**, 582 (1973).
[3] J. D. Weeks, G. H. Gilmer, and H. J. Leamy, Structural transition in the Ising-model interface, Phys. Rev. Lett. **31**, 549 (1973).
[4] S. T. Chui and J. D. Weeks, Phase transition in the two-dimensional Coulomb gas, and the interfacial roughening transition, Phys. Rev. B **14**, 4978 (1976).
[5] H. van Beijeren, Exactly solvable model for the roughening transition of a crystal surface, Phys. Rev. Lett. **38**, 993 (1977).
[6] M. Hasenbusch, S. Meyer, and M. Pütz, The roughening transition of the three-dimensional Ising interface: A Monte Carlo study, J. Stat. Phys. **85**, 383 (1996).
[7] S. Balibar, H. Alles, and A. Y. Parshin, The surface of helium crystals, Rev. Mod. Phys. **77**, 317 (2005).
[8] D. S. Fisher and J. D. Weeks, Shape of crystals at low temperatures: Absence of quantum roughening, Phys. Rev. Lett. **50**, 1077 (1983).
[9] E. Fradkin, Roughening transition in quantum interfaces, Phys. Rev. B **28**, 5338 (1983).
[10] M. Lüscher, Symmetry-breaking aspects of the roughening transition in gauge theories, Nucl. Phys. **B180**, 317 (1981).
[11] T. A. Cochran *et al.*, Visualizing dynamics of charges and strings in $(2+1)$D lattice gauge theories, arXiv:2409.17142.
[12] B. Kloss, D. R. Reichman, and Y. B. Lev, Studying dynamics in two-dimensional quantum lattices using tree tensor network states, SciPost Phys. **9**, 070 (2020).
[13] L. Pavešić, D. Jaschke, and S. Montangero, Constrained dynamics and confinement in the two-dimensional quantum Ising model, Phys. Rev. B **111**, L140305 (2025).
[14] W. Krinitsin, N. Tausendpfund, M. Heyl, M. Rizzi, and M. Schmitt, Time evolution of the quantum Ising model in two dimensions using tree tensor networks, arXiv:2505.07612.
[15] M. Moeckel and S. Kehrein, Interaction quench in the Hubbard model, Phys. Rev. Lett. **100**, 175702 (2008).
[16] S. Moudgalya, B. A. Bernevig, and N. Regnault, Quantum many-body scars and Hilbert space fragmentation: A review of exact results, Rep. Prog. Phys. **85**, 086501 (2022).
[17] M. Greiner, O. Mandel, T. W. Hänsch, and I. Bloch, Collapse and revival of the matter wave field of a Bose–Einstein condensate, Nature (London) **419**, 51 (2002).
[18] I. M. Georgescu, S. Ashhab, and F. Nori, Quantum simulation, Rev. Mod. Phys. **86**, 153 (2014).
[19] T. Kinoshita, T. Wenger, and D. S. Weiss, A quantum Newton's cradle, Nature (London) **440**, 900 (2006).
[20] E. A. Martinez, C. A. Muschik, P. Schindler, D. Nigg, A. Erhard, M. Heyl, P. Hauke, M. Dalmonte, T. Monz, P. Zoller, and R. Blatt, Real-time dynamics of lattice gauge theories with a few-qubit quantum computer, Nature (London) **534**, 516 (2016).
[21] J.-Y. Choi, S. Hild, J. Zeiher, P. Schauß, A. Rubio-Abadal, T. Yefsah, V. Khemani, D. A. Huse, I. Bloch, and C. Gross, Exploring the many-body localization transition in two dimensions, Science **352**, 1547 (2016).
[22] C. Gross and I. Bloch, Quantum simulations with ultracold atoms in optical lattices, Science **357**, 995 (2017).
[23] P. Jurcevic, H. Shen, P. Hauke, C. Maier, T. Brydges, C. Hempel, B. P. Lanyon, M. Heyl, R. Blatt, and C. F. Roos, Direct observation of dynamical quantum phase transitions in an interacting many-body system, Phys. Rev. Lett. **119**, 080501 (2017).
[24] H. Bernien, S. Schwartz, A. Keesling, H. Levine, A. Omran, H. Pichler, S. Choi, A. S. Zibrov, M. Endres, M. Greiner, V. Vuletić, and M. D. Lukin, Probing many-body dynamics on a 51-atom quantum simulator, Nature (London) **551**, 579 (2017).
[25] J. Zhang, G. Pagano, P. W. Hess, A. Kyprianidis, P. Becker, H. Kaplan, A. V. Gorshkov, Z.-X. Gong, and C. Monroe, Observation of a many-body dynamical phase transition with a 53-qubit quantum simulator, Nature (London) **551**, 601 (2017).
[26] M. Gärttner, J. G. Bohnet, A. Safavi-Naini, M. L. Wall, J. J. Bollinger, and A. M. Rey, Measuring out-of-time-order correlations and multiple quantum spectra in a trapped-ion quantum magnet, Nat. Phys. **13**, 781 (2017).
[27] S. Choi, J. Choi, R. Landig, G. Kucsko, H. Zhou, J. Isoya, F. Jelezko, S. Onoda, H. Sumiya, V. Khemani, C. von Keyserlingk, N. Y. Yao, E. Demler, and M. D. Lukin, Observation of discrete time-crystalline order in a disordered dipolar many-body system, Nature (London) **543**, 221 (2017).
[28] H. Levine, A. Keesling, A. Omran, H. Bernien, S. Schwartz, A. S. Zibrov, M. Endres, M. Greiner, V. Vuletić, and M. D. Lukin, High-fidelity control and entanglement of Rydberg-atom qubits, Phys. Rev. Lett. **121**, 123603 (2018).
[29] S. Hild, T. Fukuhara, P. Schauß, J. Zeiher, M. Knap, E. Demler, I. Bloch, and C. Gross, Far-from-equilibrium spin transport in Heisenberg quantum magnets, Phys. Rev. Lett. **113**, 147205 (2014).
[30] D. Barredo, V. Lienhard, S. de Léséleuc, T. Lahaye, and A. Browaeys, Synthetic three-dimensional atomic structures assembled atom by atom, Nature (London) **561**, 79 (2018).
[31] T. Manovitz, S. H. Li, S. Ebadi, R. Samajdar, A. A. Geim, S. J. Evered, D. Bluvstein, H. Zhou, N. U. Koyluoglu, J. Feldmeier, P. E. Dolgirev, N. Maskara, M. Kalinowski, S. Sachdev, D. A. Huse, M. Greiner, V. Vuletić, and M. D. Lukin, Quantum coarsening and collective dynamics on a programmable quantum simulator, Nature (London) **638**, 86 (2025).
[32] H. W. J. Blöte and Y. Deng, Cluster Monte Carlo simulation of the transverse Ising model, Phys. Rev. E **66**, 066110 (2002).
[33] F. Balducci, A. Gambassi, A. Lerose, A. Scardicchio, and C. Vanoni, Localization and melting of interfaces in the two-dimensional quantum Ising model, Phys. Rev. Lett. **129**, 120601 (2022).
[34] F. Balducci, A. Gambassi, A. Lerose, A. Scardicchio, and C. Vanoni, Interface dynamics in the two-dimensional quantum Ising model, Phys. Rev. B **107**, 024306 (2023).
[35] See Supplemental Material at http://link.aps.org/supplemental/10.1103/9bsk-x9rw for further details about the tree tensor network simulations, properties of the kink operator, the transfer matrix analysis, and the quantum Monte Carlo simulations.

[36] A. A. Abul-Magd and A. Y. Abul-Magd, Unfolding of the spectrum for chaotic and mixed systems, Physica (Amsterdam) **396A**, 185 (2014).
[37] Y. Y. Atas, E. Bogomolny, O. Giraud, and G. Roux, Distribution of the ratio of consecutive level spacings in random matrix ensembles, Phys. Rev. Lett. **110**, 084101 (2013).
[38] P. Silvi, F. Tschirsich, M. Gerster, J. Jünemann, D. Jaschke, M. Rizzi, and S. Montangero, The tensor networks anthology: Simulation techniques for many-body quantum lattice systems, SciPost Phys. Lect. Notes **8** (2019).
[39] J. Haegeman, J. I. Cirac, T. J. Osborne, I. Pižorn, H. Verschelde, and F. Verstraete, Time-dependent variational principle for quantum lattices, Phys. Rev. Lett. **107**, 070601 (2011).
[40] J. Haegeman, C. Lubich, I. Oseledets, B. Vandereycken, and F. Verstraete, Unifying time evolution and optimization with matrix product states, Phys. Rev. B **94**, 165116 (2016).
[41] V. Zauner-Stauber, L. Vanderstraeten, M. T. Fishman, F. Verstraete, and J. Haegeman, Variational optimization algorithms for uniform matrix product states, Phys. Rev. B **97**, 045145 (2018).
[42] H. G. Evertz, G. Lana, and M. Marcu, Cluster algorithm for vertex models, Phys. Rev. Lett. **70**, 875 (1993).
[43] H. G. Evertz, The loop algorithm, Adv. Phys. **52**, 1 (2003).
[44] S. Hearth, IsingMonteCarlo (2024).
[45] S. Sachdev, *Quantum Phase Transitions*, 2nd ed. (Cambridge University Press, Cambridge, England, 2011).
[46] E. Fradkin and L. Susskind, Order and disorder in gauge systems and magnets, Phys. Rev. D **17**, 2637 (1978).
[47] A. Hasenfratz, E. Hasenfratz, and P. Hasenfratz, Generalized roughening transition and its effect on the string tension, Nucl. Phys. **B180**, 353 (1981).
[48] S. L. Sondhi, S. M. Girvin, J. P. Carini, and D. Shahar, Continuous quantum phase transitions, Rev. Mod. Phys. **69**, 315 (1997).
[49] M. Hasenbusch, The two-dimensional XY model at the transition temperature: A high-precision Monte Carlo study, J. Phys. A **38**, 5869 (2005).
[50] J. A. Cuesta and A. Sánchez, General non-existence theorem for phase transitions in one-dimensional systems with short range interactions, and physical examples of such transitions, J. Stat. Phys. **115**, 869 (2004).
[51] W.-C. Yueh and S. S. Cheng, Explicit eigenvalues and inverses of tridiagonal toeplitz matrices with four perturbed corners, ANZIAM J. **49**, 361 (2008).
[52] J. Zeiher, J. Y. Choi, A. Rubio-Abadal, T. Pohl, R. van Bijnen, I. Bloch, and C. Gross, Coherent many-body spin dynamics in a long-range interacting Ising chain, Phys. Rev. X **7**, 041063 (2017).
[53] H. Bernien, S. Schwartz, A. Keesling, H. Levine, A. Omran, H. Pichler, S. Choi, A. S. Zibrov, M. Endres, M. Greiner, V. Vuletić, and M. D. Lukin, Probing many-body dynamics on a 51-atom quantum simulator, Nature (London) **551**, 579 (2017).
[54] P. Scholl, M. Schuler, H. J. Williams, A. A. Eberharter, D. Barredo, K.-N. Schymik, V. Lienhard, L.-P. Henry, T. C. Lang, T. Lahaye, A. M. Läuchli, and A. Browaeys, Quantum simulation of 2d antiferromagnets with hundreds of Rydberg atoms, Nature (London) **595**, 233 (2021).
[55] S. Coleman, Fate of the false vacuum: Semiclassical theory, Phys. Rev. D **15**, 2929 (1977).
[56] G. Lagnese, F. M. Surace, M. Kormos, and P. Calabrese, False vacuum decay in quantum spin chains, Phys. Rev. B **104**, L201106 (2021).
[57] A. Milsted, J. Liu, J. Preskill, and G. Vidal, Collisions of false-vacuum bubble walls in a quantum spin chain, PRX Quantum **3**, 020316 (2022).
[58] A. Zenesini, A. Berti, R. Cominotti, C. Rogora, I. G. Moss, T. P. Billam, I. Carusotto, G. Lamporesi, A. Recati, and G. Ferrari, False vacuum decay via bubble formation in ferromagnetic superfluids, Nat. Phys. **20**, 558 (2024).
[59] N. Tausendpfund, M. Rizzi, W. Krinitsin, and M. Schmitt, TTN—A tree tensor network library for calculating ground-states and solving time evolution (2024), available on Zenodo.
[60] M. Fishman, S. R. White, and E. M. Stoudenmire, The ITensor software library for tensor network calculations, SciPost Phys. Codebases **4** (2022).
[61] B. Bauer *et al.*, The ALPS project release 2.0: Open source software for strongly correlated systems, J. Stat. Mech. (2011) P05001.
[62] www.gauss-centre.eu
[63] Jülich Supercomputing Centre, JUWELS cluster and booster: Exascale pathfinder with modular supercomputing architecture at JSC, J. Large-Scale Res. Facil. **7**, A183 (2021).
[64] Jülich Supercomputing Centre, JURECA: Data centric and booster modules implementing the modular supercomputing architecture at JSC, J. Large-Scale Res. Facil. **7**, A182 (2021).
[65] W. Krinitsin, N. Tausendpfund, M. Rizzi, M. Heyl, and M. Schmitt, Data and code associated to the paper roughening dynamics of interfaces in two-dimensional quantum matter, 10.5281/zenodo.14705609 (2025).

End Matter

BKT transition of the SOS model—Here, we demonstrate that the nature of the transition in the effective SOS model (3) belongs to the BKT universality class. To this end, we use the VUMPS algorithm [39–41] to study the ground state properties of the effective model. This allows us to work directly in the thermodynamic limit with a fixed truncation of bosonic excitations $N_{\max} \in 2\mathbb{Z}$. In the two-dimensional model, this is equivalent to considering an infinitely long slab of width $L_y = N_{\max} + 1$ with the interface oriented along the infinite direction. To observe the critical properties, it is necessary to scale the results against $N_{\max} \to \infty$.

In practice, we considered $N_{\max} \leq 14$. Since the local Hilbert space scales as $\dim(\mathcal{H}_{\mathrm{loc}}) = N_{\max} + 1$, a maximum bosonic occupation of 14 already leads to very long simulation times of 13×10^3 s per iteration for a bond dimension of $\chi = 600$.

In contrast to continuous phase transitions described by the Landau-Ginzburg theory, the BKT transition cannot be detected by the divergence of any derivative of the energy

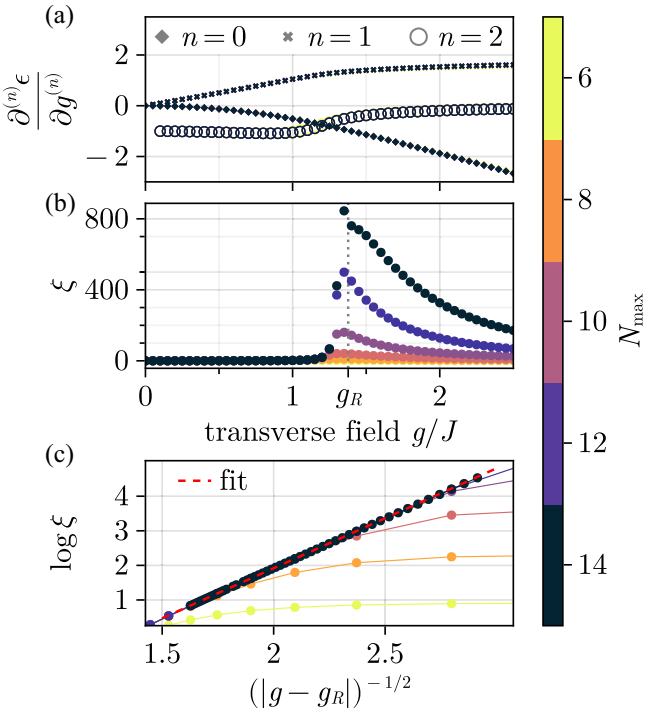

FIG. 4. (a) The energy density and its first two derivatives with respect to the transverse field g, as a function of g. All of the different orders do not show any sign of nonanalyticity around the transition point, excluding the possibility of it being a first or second order phase transition. (b) The correlation length shows a divergence at $g = g_R$ when increasing the maximal bosonic occupation number. All results are obtained with a bond dimension of $\chi = 600$ and are converged for $N_{\max} < 14$. For the $N_{\max} = 14$, the points around the transition are not yet fully converged, showing numerical artifacts for $g > g_R$. (c) Fit of (A1) to the data, showing the correct BKT type divergence law of the correlation length. Increasing $N_{\max}$ again leads to a better agreement between the data and the expected law. The critical transverse field obtained from the fit for the largest $N_{\max} = 14$ is $g_R/J = 1.38$.

density $\epsilon(g)$, which is an analytical function of g. This is demonstrated in Fig. 4(a) via the example of the first and second derivative of $\epsilon(g)$. Moreover, we observe that $\epsilon(g)$ and its derivatives are quickly converging in $N_{\max}$.

Characteristic of the BKT transition is the exponential divergence of the correlation length when approaching the critical value g_R,

$$\xi(g) = \xi_0 \exp\left(\frac{B}{\sqrt{|g-g_R|}}\right), \quad \text{for } g < g_R. \tag{A1}$$

Here, ξ_0 and B are nonuniversal constants depending on the model and on the observable used to extract the correlation length. We observed the largest correlation length for the vortex-vortex correlation function

$$C(l) = \langle e^{-iN_0} e^{iN_l} \rangle \overset{l\to\infty}{\to} A e^{-\frac{l}{\xi}} + C_\infty,$$

which is closely related to the kink operator (4). The constant C_∞ is expected to be close to 1 in the $g < g_R$ region, while we expect it to vanish after the BKT transition for $N_{\max} \to \infty$. In particular one has $\langle K_\alpha(l)\rangle \to |C_\infty|$ for $l \to \infty$. The results are displayed in Fig. 4(b) for $6 \le N_{\max} \le 14$. For increasing $N_{\max}$, the correlation length shows a divergent behavior around $g/J \approx 1.4$ with $\xi \sim 800$ for $N_{\max} = 14$.

To quantify that $\xi(g)$ has the correct behavior approaching g_R/J, we fit $\xi(g)$ for $N_{\max} = 14$ for $1.1 < g/J < 1.385$ with higher resolution using Eq. (A1). From this fit, we obtain $g_R/J \approx 1.38$. In Fig. 4(c) we plot the logarithmic correlation length as a function of $1/\sqrt{|g-g_R|}$ for $g < g_R$ and $6 \le N_{\max} \le 14$ using the value of g_R obtained by the fit. Increasing $N_{\max}$ leads to a better agreement between the data and the prediction for the correlation length, which should be exact in the limit $N_{\max} \to \infty$. For lower $N_{\max}$ the curve starts flattening out and thus deviating sooner, illustrating the finite $N_{\max}$ effects.

Finite temperature crossover in the classical limit—In the classical limit $g \to 0$ the effective model (3) contains only commuting operators $|N_j - N_{j+1}|$. Thus, all eigenstates are simply given by product states $|\{s_j\}\rangle$, fixing the occupation on the jth site. To study the thermodynamic properties in this limit, it is sufficient to replace the number operator N_j by its eigenvalues $s_j \in \{0, N_{\max}\}$,

$$\mathcal{H}_{\text{class}}(\{s_j\}) = 2J \sum_{j=1}^{L_x-1} |s_j - s_{j+1}| = \sum_{j=1}^{L_x-1} h(s_j, s_{j+1}). \tag{B1}$$

Let $V_{s,s'} = \exp[-\beta h(s,s')]$ be the transfer matrix of the classical system and define the general α twisted boundary vector $|E(\alpha)\rangle = \sum_{s=0}^{N_{\max}} e^{i\alpha s}|s\rangle$. The α twisted partition function of a chain of length L_x with open boundary conditions can be written compactly as

$$\begin{aligned}\mathcal{Z}(\alpha) &= \sum_{s_1=0}^{N_{\max}} \cdots \sum_{s_{L_x}=0}^{N_{\max}} e^{-\beta \mathcal{H}_{\text{class}}(\{s_j\}) - i\alpha(s_1 - s_{L_x})} \\ &= \langle E(\alpha)|V^{L_x-1}|E(\alpha)\rangle. \end{aligned} \tag{B2}$$

The standard partition function corresponds to zero twisting, i.e., $\mathcal{Z} = \mathcal{Z}(0)$. We can now write down the expectation value of the string operator $\langle K_l\rangle$. For simplicity, we consider $l = L_x$, i.e., the end-to-end expectation value. Using the twisted partition function, we obtain

$$\langle K_\alpha(L_x)\rangle = \frac{\mathcal{Z}(\alpha)}{\mathcal{Z}(0)}. \tag{B3}$$

The calculation can be further simplified by diagonalizing the transfer matrix $V = U\Lambda U^\dagger$. In this case, the

twisted partition function can be written as

$$\mathcal{Z}(\alpha) = \lambda_1^{L_x-1} \sum_{s=0}^{N_{\max}} f_n^{L_x-1} |c_n(\alpha)|^2, \tag{B4}$$

where λ_1 is the largest eigenvalue, $f_n = \lambda_n/\lambda_1$, and $c_n(\alpha)$ are the form factors obtained by calculating the overlap between the eigenstates $|\psi_n\rangle$ of V and the twisted boundary vector $|E(\alpha\rangle$.

Numerically we found the operator $\langle K_\alpha(L_x)\rangle$ to rapidly converge in $N_{\max}$; more specifically $N_{\max} = 200$ is large enough for our analysis (see SM [35] for more details).

It is also possible to understand the crossover behavior analytically and derive a functional form for the transition temperature $T_R(L_x)$. Using the exact eigenvectors and eigenvalues of the transfer matrix V of the classical model (B1), we were able to find an approximation of the end-to-end string operator in the limit of large $N_{\max}, L_x \gg 1$, and small $q \ll 1$ [35],

$$\langle K_\alpha(L_x)\rangle \approx \exp\left(-2q(1-\cos(\alpha)L_x\right). \tag{B5}$$

By setting $\langle K_\alpha(L_x)\rangle = 1/2$ and solving for $T/J = -2/\log(q)$, we find that the transition temperature T_R should vanish logarithmically with the system size L_x,

$$T_R(L_x)/J = 2\log\left(\frac{2[1-\cos(\alpha)]L_x}{\log(2)}\right)^{-1}, \tag{B6}$$

which has been confirmed numerically; see inset of Fig. 2(c).